Journal of Energy Storage 41 (2021) 102979

Contents lists available at ScienceDirect

Journal of Energy Storage

journal homepage: www.elsevier.com/locate/est

Improved battery performance of silicon modified $Na_{0.67}Fe_{0.5}Mn_{0.5}O_2$ and its structural and electrochemical properties: An investigation of infrared thermal imaging

S. Altin [a,b,*], E. Altundag [a], E. Altin [c], S. Altundag [b]

[a] Inonu University, Energy Science and technology division, 44280, Malatya Turkey
[b] Inonu University, Physics Department, 44280, Malatya Turkey
[c] Inonu University, IBTAM, 44280, Malatya, Turkey

ARTICLE INFO

Keywords:
$Na_{0.67}Fe_{0.5}Mn_{0.5}O_2$
Si-modification
in-situ IR-thermal imaging

ABSTRACT

Here, we present a systematically Si-doping strategy to improve the structural stability and battery performances of P2-type $Na_{0.67}Mn_{0.5}Fe_{0.5}O_2$ samples. Through Si^{4+} doping intended to settlement of the interstitial region in the crystal structure and investigate the effect on the electrical conductivity of the $Na_{0.67}Mn_{0.5}Fe_{0.5}O_2$. The structural properties were examined by x-ray absorption near-edge structure (XANES), x-ray diffraction (XRD), Scanning Electron Microscopy (SEM) and Fourier transform infrared spectroscopy (FTIR) measurements. The XANES spectra showed that the valence of both Manganese and iron ions was unchanged by Si. According to charge/discharge cycling measurements for constant current at room temperature, the lowest capacity fade was obtained for $Na_{0.67}Mn_{0.5}Fe_{0.48}Si_{0.02}O_2$. The cycling measurements were also investigated at 50°C, and it was observed that the electrochemical properties were changed with temperature. It was developed an experimental setup for the measurements of the internal temperature of the battery cells during the charging/discharging process of CR2032 coin cells using an infrared thermal camera. The ohmic heat was calculated from chronoamperometry measurements using a developed setup, and the heat generation was explained by a quadratic equation in the system.

1. Introduction

Na-based power technology is at the beginning of commercialisation. Scientific studies about the development of Na batteries have focused on Li-based metal oxide materials. There are a lot of information available about Li-based metal oxide cathode materials, and it is well known that the chemical compositions and structures of Li metal oxides are similar to Na oxides [1–9].

Although Li-ion batteries are very common in daily life, Na-ion battery studies have attracted attention due to the abundance of Na resources, low toxicity, low cost, and similar intercalation chemistry. Among the Na-based cathode materials, $Na_{0.67}Fe_{0.5}Mn_{0.5}O_2$ cathode materials have received the most attention since their components are cheaper than materials that consist of Co, Mn, etc. [10–12]. Yabauuchi et al. discovered the $Na_{0.67}Fe_{0.5}Mn_{0.5}O_2$ system in 2012 and two types of crystal structures, named P2-type with P63mmc symmetry and O3-type with *R-3m* symmetry, were found [13]. The half-cell capacity reached 190 mAh/g in the range of 1.5–4.3 V for low applied current [14].

It is known that the partial chemical substitutions of a transition metal site by the other appropriate elements in the periodic table represent a challenge in the battery studies. It is well known that a small substitution with impure ions in the structure may change the volume, electrostatic interactions, and movements of Na ions during the charge/discharge process. When examining the structural modification of $Na_{0.67}Fe_{0.5}Mn_{0.5}O_2$ materials, limited studies were found including the substitution elements of Cr, Ti, Al, Ni, V, Mg, etc. [15–29]. Although there were chemical substitutions of both Fe and Mn in the structure, Mn and Fe share the same positions in the lattice of $Na_{0.67}Fe_{0.5}Mn_{0.5}O_2$

Herein, the Fe site of $Na_{0.67}Fe_{0.5}Mn_{0.5}O_2$ materials was substituted with Si by a modified solid-state reaction with quenching at high temperatures. The structural morphology of the fabricated powders was determined by FTIR, SEM, XRD, and XAS measurements. The produced powders were used as a cathode material for CR2032 coin cells, and the electrochemical properties and battery performance were investigated.

* Corresponding author.
E-mail address: serdar.altin@inonu.edu.tr (S. Altin).

https://doi.org/10.1016/j.est.2021.102979
Received 9 January 2021; Received in revised form 3 July 2021; Accepted 21 July 2021
Available online 29 July 2021
2352-152X/© 2021 Elsevier Ltd. All rights reserved.

It was found that $Na_{0.67}Mn_{0.5}Fe_{0.48}Si_{0.02}O_2$ shows the best performance among the other substitution levels. In situ infra-red (IR) thermal imaging was done on the best-performing cells and it was found that the heat generation exhibited a quadratic dependence in the cells.

2. Experimental section

$Na_{0.67}Mn_{0.5}Fe_{0.5-x}Si_xO_2$ materials (where x=0, 0.02, 0.04, 0.06, 0.08, and 0.10) were fabricated using Na_2O_2, Fe_2O_3, SiO_2, and Mn_2O_3 as starting powders. The starting materials were weighed on a sensitive balance (Radwag) and mixed in an agate mortar for 1–1.5 h in a glove box filled with argon gas. Then, the powders were done pellets by pressing under 5 tons. The produced pellets were placed in a tube furnace and heat-treated at 1000°C for 12 h under ambient conditions, and placed in L-N2 for quenching.

The XRD patterns of the samples were determined by a Rigaku RadB Dmax diffractometer using CuK_α ($\lambda_{K\alpha}$=1.5405 Å) radiation. The GSAS-II open-source program was used for the calculation of the lattice parameters of the powders fabricated [30,31]. FTIR spectra of the samples were measured with a Perkin Elmer spectrometer (Spectrum One model) in the range of 400–4000 cm^{-1}. XAS experiments were performed in the XRF/XAFS Beamline at SESAME-Jordan. The SEM images of the samples were taken by a Leo EVO-40 VPX.

The Si-substituted powders were used for the production of cathodes. For this purpose, the active materials, carbon black, and polyvinylidene difluoride (PVDF) (70:15:15) were mixed in NMP solvent for overnight stirring. The obtained mixtures were used for the film fabrication onto Al foil. A doctor blade with a coating size of 100 μm was used for the production of the cathodes. After production of the films, they were inserted into a vacuum oven at 110°C overnight. The pre-fabricated cathodes were compressed with a rolling press for higher density and better electrical conductivity. The pressed cathodes were punched with a diameter of 10 mm, and inserted in the glove box (Inert Technology, I-Lab). The mass of $Na_{0.67}Mn_{0.5}Fe_{0.5-x}Si_xO_2$ on punched cathodes was in the range of 2.2–3.1 mg. The half cell configuration was used for the battery tests and elemental Na was used as an anode in the cells. The 1 M $NaClO_4$ in PC/EC (50/50 w/w) was preferred as an electrolyte in the battery cells.

CV experiments of the CR2032 coin cells were performed in a voltage range of 1.5–4.0 V using a scan rate of 0.1 mV s^{-1} to determine the anodic and cathodic reactions in the cells. The charging/discharging measurements for up to 100 cycles for constantly applied currents were determined using the same voltage range. The C/3 rate was used for the current density, and the measurements were performed with an Ivium Octostat30 potentiostat at room temperature. The temperature dependence of the cycling measurements of the cells was performed with a Zive SP1 integrated NUVE EN-120 incubator.

In situ thermal imaging of the cell was performed using a designed CR2032 coin cell, as given in Scheme 1. The $Na_{0.67}Mn_{0.5}Fe_{0.48}Si_{0.02}O_2$ was used for the measurements. The bottom case of the CR2032 coin cell was drilled to make a hole by the press with radii of 4 mm and the glass with a thickness of 40 μm and radii of 12 mm were pasted over the hole region of the bottom case of the cell by UHU plus 40281 and cured 24 h. As a current collector, the Al was coated onto the glass/drilled CR2032 bottom case by the Vaksis-Midas PVD/4T thermal evaporator, and the thickness of the Al was 300 nm. The cathode mixture was coated onto the Al/glass/drilled CR2032 bottom case, and it was dried in a vacuum furnace at 120°C for 24 h. The cathode/Al/glass/drilled CR2032 bottom case was used for making the CR2032 coin cell. Fluke TiS60+ was used for the IR thermal imaging of the samples. It should be noted that the cell design is similar to in-situ CR2032 coin cells [32].

The designed CR2032 cell was inserted into a thermally insulated box and the IR thermal camera was placed across the cell, as seen in Scheme 1. First, the battery cell was charged at 4 V for 3 h and then discharged at 1.5 V for 3 h. During the charging and discharging process, IR thermal imaging of the drilled region was performed every 10 min.

3. Results and discussion

3.1. Structural properties

The XRD patterns of the Si-modified $Na_{0.67}Fe_{0.5}Mn_{0.5}O_2$ are presented in Fig. 1a. It was found that the unsubstituted sample was well fitted with $Na_{0.67}Fe_{0.5}Mn_{0.5}O_2$ and impurity phases were not observed following Si substitution in the structure. The XRD patterns of the samples were analyzed by open-source GSAS-II and the obtained curve of the x=0.02 sample, as an example, is seen in Fig. 1b. The refinement process was performed using the hexagonal structure and P63/mmc space group. The difference profile (Diff.) between the observed (Obs.) and calculated (Calc.) diffraction pattern was given at the bottom of the plot in Fig. 2.b. A good fit was obtained with R factors, $W_R = 18.8$ % and $R_f = 12.4$ %.The lattice parameters of the samples are given in Table 1, and the undoped sample has similar structural parameters as those found in the previous studies [26,18]. While the a-lattice parameter decreased, the c-lattice parameter and c/a ratio increased by increasing Si content in the materials and the lattice volume decreased. The ionic radii of the elements were equal to 0.26 Å for Si^{4+}, (0.72 Å for low spin and 0.785 Å for high spin) for Mn^{3+}, (0.67 Å) for Mn^{4+}, (0.69 Å for Low Spin (LS) and 0.785 Å for high spin (HS)) for Fe^{3+} and (0.725 Å) for Fe^{4+} in the structure of $Na_{0.67}Fe_{0.5}Mn_{0.5}O_2$. Therefore, there are two scenarios for the settlement of Si ions: Si^{4+} ions may locate the interstitial site in the lattice, which causes an increase in the volume of the cells, and Si^{4+} ions may not diffuse in the lattice and cause the formation of a secondary phase. In the second case, we expected to see an impurity phase in the XRD pattern result which was not observed, but there was a broad halo indicated in Fig. 1 with the turquoise color. The increasing of the c-lattice parameter may be related to the settlement of Si ions in the interstitial region of the crystal structure but the Si ions in the interstitial region should be less than that of the doping content since there is also a broad peak in the XRD pattern which may be associated with the formation of amorphous Si- phases. The decrease of the a-lattice parameters may be explained by the formation of the electrical attractive force of Si^{4+} ions for the first neighboring ions around them.

Fig. 2 presents the FTIR spectra of Si-modified $Na_{0.67}Fe_{0.5}Mn_{0.5}O_2$ powders, and the characteristic bands at 601 cm^{-1} (P_1) are explained by the bond of Fe–O bonds and the bending of Na–O bonds [33]. The small bands at 750 cm^{-1} (P_2) are due to Mn – O vibrations [34] and the bands around 874cm^{-1} (P_3) is related to the bond of Fe–O–Fe [35]. The other bands between 1250 and 1750 cm^{-1} (P_4 and P_5) are due to Mn – O and Fe – O [36,37]. The FTIR bands of Si–O were observed at 450 cm^{-1} (rocking of Si–O) 820 cm^{-1} (bending of Si–O), and 1040 cm^{-1} (stretching of Si–O–Si) [38] and the SiO bands in this study overlapped with Fe–O and Mn–O in the spectrum.

Fig. 3a–f present the surface morphology of Si-modified $Na_{0.67}Fe_{0.5}Mn_{0.5}O_2$ powders. The undoped sample showed a grain size of around 0-1 μm and the grains stuck together with random orientation. The Si modification up to x=0.4 caused an increase in the stacking formation by cornered grains and the further increase in Si ions shows the formation of the smaller grains in the structure. Therefore the grain formation of Si on $Na_{0.67}Fe_{0.5}Mn_{0.5}O_2$ behaves like a film coating on the grains and it may result in the change in the diffusion paths of Na ions, which is discussed in the electrochemical section.

It is well known that a change in the valence state of the transition metals in battery cells is an important parameter for cell performance. For this purpose, we measured the XANES K-edges spectra of Mn (6539 eV) and Fe (7112 eV) as seen in Fig. 4a and 4b. The effect of Si ions in $Na_{0.67}Fe_{0.5}Mn_{0.5}O_2$ was investigated to understand the redox mechanism. No differences were observed in the XANES spectra by following Si modification and this demonstrates that the Si-ions did not cause the change in the valence state of the manganese and iron ions in the samples

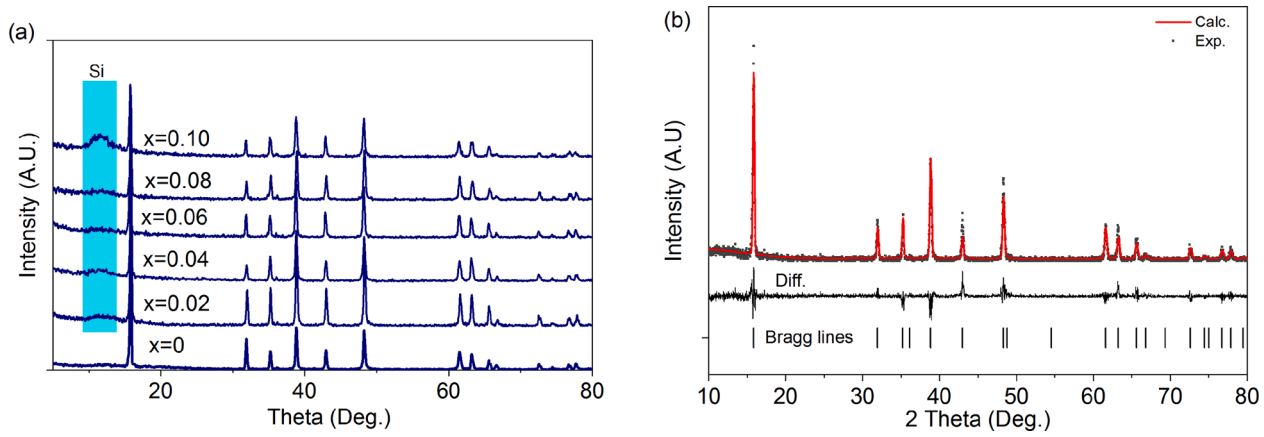


Fig. 1. (a) XRD patterns of Si-modified samples and (b) results of Rietveld refinement for x=0.02.

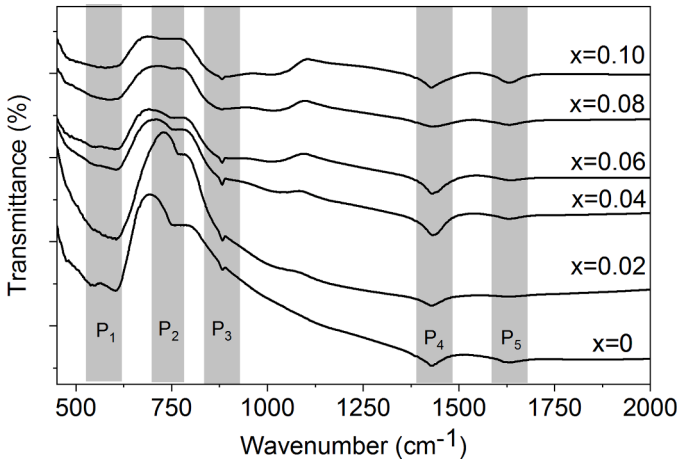


Fig. 2. FTIR of Si-modified $Na_{0.67}Fe_{0.5}Mn_{0.5}O_2$.

Table 1
Lattice parameters of Si-modified samples.

Sample	a (Å)	c (Å)	c/a	V (Å^3)
$Na_{0.67}Mn_{0.5}Fe_{0.5}O_2$	2.942041 (±0.348 × 10^{-3})	11.186415 (±0.102 × 10^{-2})	3.802263	83.853 (±0.011)
$Na_{0.67}Mn_{0.5}Fe_{0.48}Si_{0.02}O_2$	2.939736 (±0.312 × 10^{-3})	11.191619 (±0.945 × 10^{-3})	3.807015	83.761 (±0.013)
$Na_{0.67}Mn_{0.5}Fe_{0.46}Si_{0.04}O_2$	2.939813 (±0.677 × 10^{-3})	11.203338 (±0.195 × 10^{-2})	3.810990	83.853 (±0.032)
$Na_{0.67}Mn_{0.5}Fe_{0.44}Si_{0.06}O_2$	2.938086 (±0.524 × 10^{-3})	11.205923 (±0.16 × 10^{-2})	3814021	83.774 (±0.025)
$Na_{0.67}Mn_{0.5}Fe_{0.42}Si_{0.08}O_2$	2.936114 (±0.574 × 10^{-3})	11.214778) (±0.169 × 10^{-2})	3.819599	83.727 (±0.027)
$Na_{0.67}Mn_{0.5}Fe_{0.40}Si_{0.10}O_2$	2.934376 (±0.906 × 10^{-3})	11.221766 (±0.276 × 10^{-2})	3.824243	83.680 (±0.042)

3.2. Electrochemical properties

The CV measurements of the undoped and Si-modified $Na_{0.67}Mn_{0.5}Fe_{0.5}O_2$ samples for a rate of 0.1 mV/s in the range of 1.5–4.0 V are given in Fig. 5 and two wide anodic and cathodic peaks were observed. The CV data of all samples exhibit almost similar trends. It is well known that Fe and Mn ions contribute to the redox reactions in the cells. As indicated in the XRD section, Si modification affects the c/a ratio of the materials, and the distance between the layers in the lattice increased by Si-content. The change of the distance around the Na- ions in the lattice causes the change of the strength of the bonds and the electrostatic force among the ions. In this case, the energy of the redox reaction peaks changes. It was seen from Fig. 5 that the voltage of main Mn^{3+}/Mn^{4+} redox reaction peaks during to charging process decreases by increasing Si-content and it is clear that the Si-modification causes the change of the chemical potential, binding energy, and diffusion rate of Na ions in $Na_{0.67}Mn_{0.5}Fe_{0.5}O_2$ structure.

The battery performance of the cells fabricated by Si modification of $Na_{0.67}Fe_{0.5}Mn_{0.5}O_2$ samples at room temperature was investigated for up to 100 cycles using the C/3 rate and the voltage–capacity graphs of x= 0.02 is presented in Fig. 6a as an example. Fig. 6b exhibits capacity graphs that depend on the cycle number for all Si modifications and it is seen that the highest capacity value for the first cycle and the capacity fade over the 100 cycles were determined for the x=0.02 Si modification. The highest capacity value was obtained 140.9 mAh/g for x=0.02 Si modification and the capacity fade was found to be 0.296 for x=0.02 substitution, as seen in Table 2.

Fig. 7a presents the cycling measurements depending on the capacity and voltage of the cells at 50°C for x= 0.02, which has the best electrochemical properties. Fig. 7b presents the capacity measurements depending on the cycle number for x=0.02, 0.04, 0.06, 0.08, 0.10 and the details of the measurements are given in Table 2. When the measurements at 50°C were compared with measurements performed at the room temperature, it was found that there was an increase which is the expected behavior, and details regarding this can be found in previous work [39–42]. This may explain that the increase in the first capacity at 50°C may be explained by the increase in the mobility of the Na ions and this may cause fast degradation of the lattice which may result in the high capacity fade [43-46].

The rate performance of Si-modified $Na_{0.67}Fe_{0.5}Mn_{0.5}O_2$ in the 1.5–4.0 V voltage range at different current rates of C/5, C/3, C 2C, and 4C is shown in Fig. 8. While the highest capacity for C/5-rate was obtained for x=0.02 Si-content, the lowest capacity was observed for x=0.10 Si content at the same C-rate. As the C-rate increases, the capacity decrease gradually from 168.5 mAh/g at C/5 to 12 mAh/g at C/5 for x=0.02 Si content. The effect of the C-rate on the capacity of the cells is related to the dissipated energy associated with the concentration polarization in the electrodes of the cells [26]

3.3. In situ IR thermal measurements

It is well known that the heat generated during the charging and discharging process is an important problem of rechargeable batteries. Although the development of a cooling system based on the heat

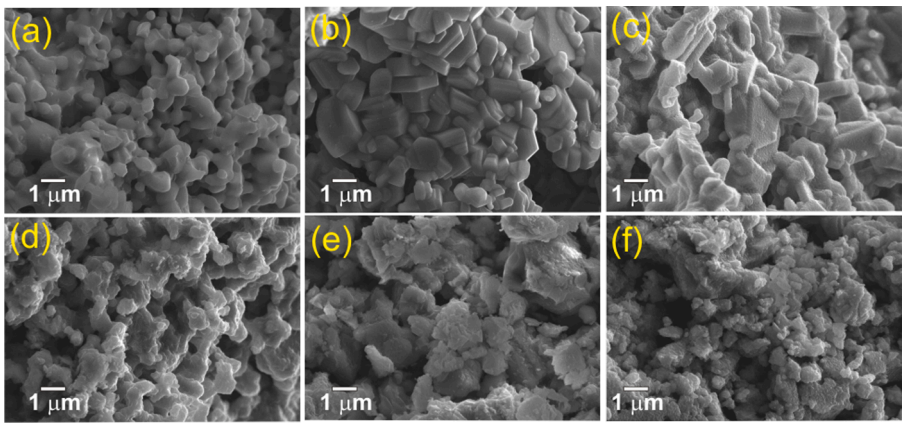


Fig. 3. SEM images of Si Modified $Na_{0.67}Fe_{0.5}Mn_{0.5}O_2$ for (a) x=0, (b) x=0.02, (c) x=0.04, (d) x=0.06, (e) x=0.08 and (f) x=0.1.

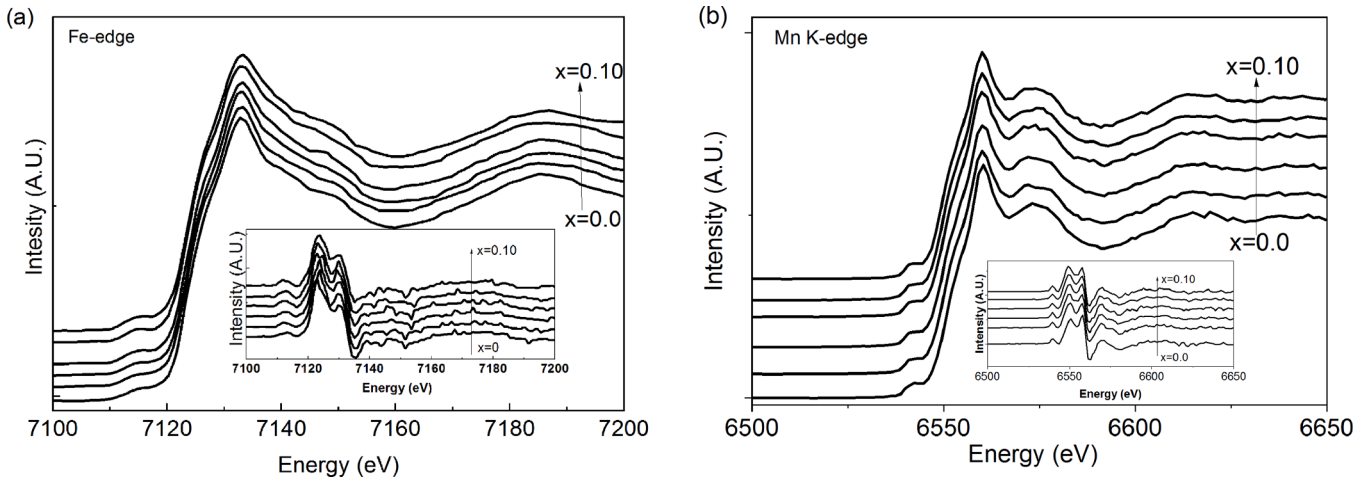


Fig. 4. XANES spectra of (a) Fe and (b) Mn for Si-modified samples.

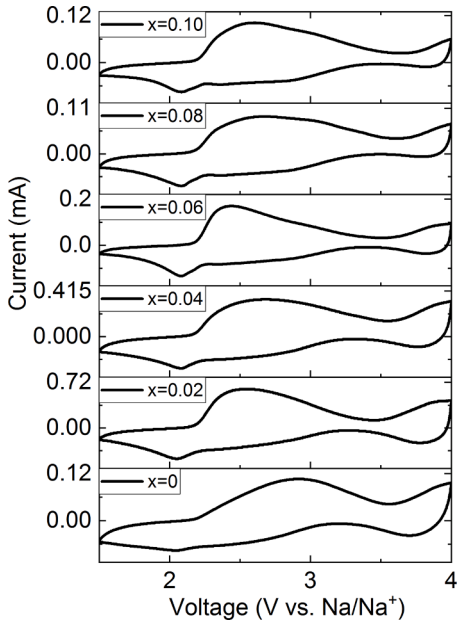


Fig. 5. CV of Si-modified $Na_{0.67}Fe_{0.5}Mn_{0.5}O_2$.

generation of battery cells has been extensively studied in the last decade, we want to present a new approach based on microscopic properties. It is well known that the generated heat spreads to all heat-conducting parts of the case of the battery cells and this can cause a misinterpretation of the real heat generated by Na/Li insertion and disinsertion in the cells. Therefore, it should develop the determination method for heat generation at the cathode region inside of the cells. For this purpose, a hole was drilled in the CR2032 coin cells and glued a glass inside region of the cell for sealing as mentioned experimental section.

Fig. 9 shows the thermal imaging of the cells and the hole region was seen in the IR image and the line analysis of the background region and coin cell region was given right and up panel of the figure. It was observed that the background temperature, coin cell temperature and temperature of the hole region were 23.5°C, 24.2°C and 25.5°C, respectively Therefore, it was observed that the temperature of the inner part of the battery cells was higher than that of environmental temperatures, which is important for the understanding the mechanism of the batteries.

It is well known that the heat of the isolated environment for batteries can be given as the following [47]:

$$\Delta Q = Q_{p-}Q_d \tag{1}$$

where Q_p and Q_d are productive and dissipation heat, respectively. It is well known that Q_p consists of reactive heat (Q_r), active polarisation heat (Q_a), ohmic heat (Q_{ohm}) and Q_d is composed of head conduction (Q_{con}) and heat radiation (Q_{rad}),as given below [48]:

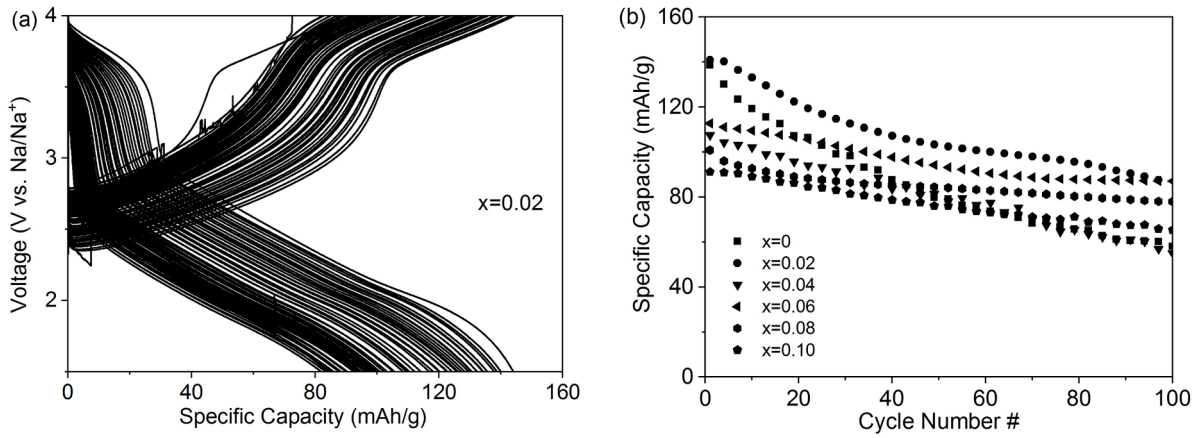


Fig. 6. Capacity- voltage graphs for (a) x=0.02 and (b) capacity-cycle graphs of Si-modified materials at room temperature.

Table 2
The electrochemical performance of the cell fabricated at room temperature and 50°C.

Temp.	Cathode	cycle	100. cycle	Capacity Fade (%)
Room Temp.	$Na_{0.67}Mn_{0.5}Fe_{0.5}O_2$	121	72	40.5
	$Na_{0.67}Mn_{0.5}Fe_{0.48}Si_{0.02}O_2$	140.9	82	41.8
	$Na_{0.67}Mn_{0.5}Fe_{0.46}Si_{0.04}O_2$	107.5	55	48.8
	$Na_{0.67}Mn_{0.5}Fe_{0.44}Si_{0.06}O_2$	112.7	87	22.8
	$Na_{0.67}Mn_{0.5}Fe_{0.42}Si_{0.08}O_2$	100.8	78	22.6
	$Na_{0.67}Mn_{0.5}Fe_{0.40}Si_{0.1}O_2$	91.2	65.3	28.4
50°C	$Na_{0.67}Mn_{0.5}Fe_{0.49}Si_{0.01}O_2$	135.8	61.3	54.8
	$Na_{0.67}Mn_{0.5}Fe_{0.47}Si_{0.03}O_2$	99.3	72.2	27.3
	$Na_{0.67}Mn_{0.5}Fe_{0.45}Si_{0.05}O_2$	102.4	39	62
	$Na_{0.67}Mn_{0.5}Fe_{0.43}Si_{0.07}O_2$	118.2	89.3	24.4
	$Na_{0.67}Mn_{0.5}Fe_{0.40}Si_{0.1}O_2$	110	78.6	28.5

$$Q_p = Q_r + Q_a + Q_{ohm} \tag{2}$$

$$Q_d = Q_{con} + Q_{rad} \tag{3}$$

The Q_r term explains the concentration differences in the cathode (or anode) and electrolyte, which cause the mass transfer in the cell and the Q_a term is due to the electrochemical reaction in the cell. The Q_{ohm} term can be explained by the ionic resistance of the electrolyte and the electronic resistance, contact resistance, etc. This term shows the ohmic behavior for the voltage and current. Therefore, the temperature changes during the charge/discharge process of the battery cells are due to heat generation, which has multiple components as indicated above.

Yang et al. stated that the temperature change in battery cells is explained by Q_a and Q_{ohm} in the cells [47]. The heat generation of battery cells can be calculated by the Bernard equation, given below [49, 50]:

$$q = I\left[(V_{oc} - V) - T\frac{dV_{oc}}{dT}\right] \tag{4}$$

where *I, V, T*, and V_{oc} are the current, voltage, temperature, and open-circuit voltage, respectively [51,52]. The first term is related to Q_{ohm} and the second term is due to Q_d, as indicated in Eq. (3).

Fig. 10a presents the Q_{ohm}–time graph of the battery cell for constant charging at 4 V and discharging at 1.5 V. It is seen that Q_{ohm} for both conditions is high and gives an almost exponential decrease with increasing time since the absolute value of the current for both conditions decreased with increasing time. Therefore, it is expected that the temperature increase for the high current region should be high and the rate of temperature change should decrease slightly with time. For this purpose, we performed in situ thermal imaging under a constant voltage of 4 V and 1.5 V, respectively and the obtained temperature differences of the cathode material and the environmental temperature are given in Fig. 10b. It is seen that the temperature increased very fast at first and then a plateau was observed due to the change of the current in the cells. The data in Fig. 10b was fitted by the polynomial function given below:

$$\Delta T(t) = B_1 \cdot t + B_2 \cdot t^2 + B_3 \cdot t^3 \tag{5}$$

where t, B_1, B_2, and B_3 are the fitting constants of Eq. (5). The fitting parameters are given in Table 3 and Adj. R-Square values show the well-

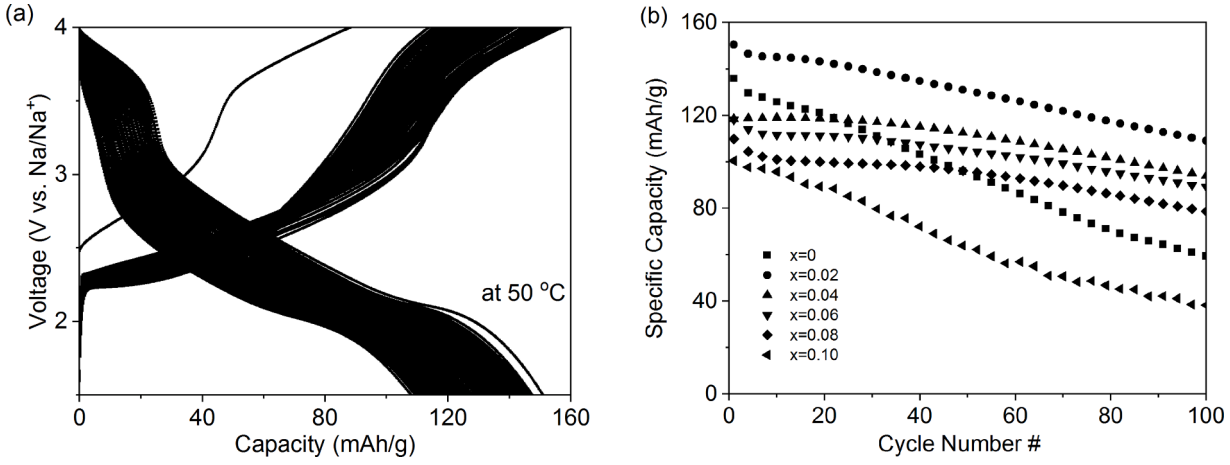


Fig. 7. Capacity- voltage graphs for x=0.02 and capacity-cycle graphs of Si-modified materials at 50°C.

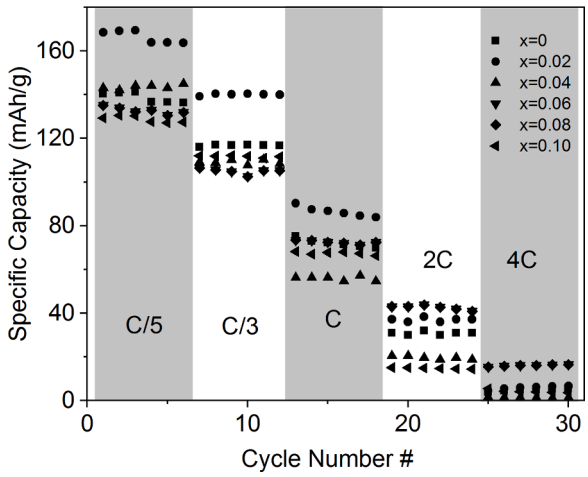


Fig. 8. C-rates of the cells fabricated.

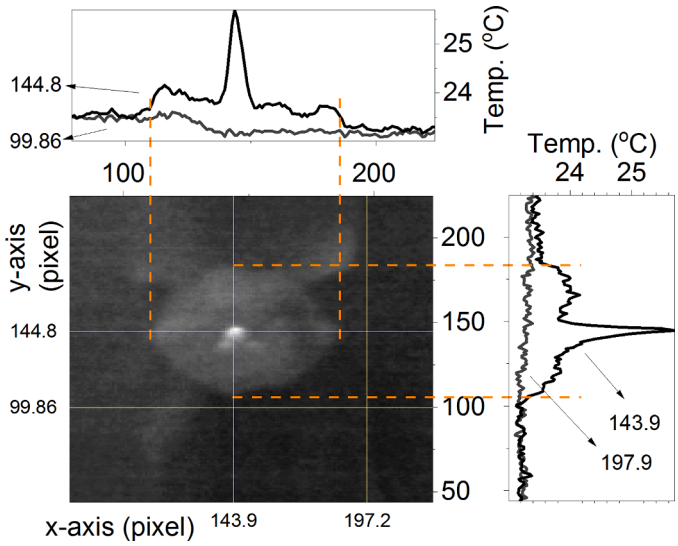


Fig. 9. as an example of IR-thermal Measurements of Voltage charge and discharge. The figure was taken during to 4V charging for 20 min.

fitting by Eq. (5). It is well known that heat generation can be calculated by the following equation:

$$q = k\frac{dT}{dt} \tag{6}$$

where k is the constant for the cells. In this case Eq. (5) was used for Eq. (6) as below:

$$q = k\left(B_1 + 2B_2 \cdot t^1 + 3B_3 \cdot t^2\right)$$

He et al. suggested a model for heat generation in the battery cells that have a quadratic form, which is similar to our study and the details can be found in previous work [52].

It is well known that there are two different types of Na sites in the P63mmc structure of $Na_{0.67}Mn_{0.5}Fe_{0.5}O_2$ [53-55] and the reaction mechanism can be given by the following [18]:

$$Na_{0.67}Mn_{0.5}Fe_{0.5}O_2 \xrightarrow{first\ \ reaction} Na_{0.20}Mn_{0.5}Fe_{0.5}O_2 + 0.47Na^+ + Q_1(heatgeneration)$$

$$Na_{0.20}Mn_{0.5}Fe_{0.5}O_2 \xrightarrow{second\ \ reaction} Mn_{0.5}Fe_{0.5}O_2 + 0.2Na^+ + Q_2(heatgeneration)$$

Therefore, the reactions above cause the formation of heat in the cells, and the Q_1 and Q_2 energies are the sources of the temperature increase in the structure. The binding energy in the first Na site in the lattice should be lower than that of the second Na site, which was obtained in the second reaction in the lattice since the number of Na ions in the first reaction was higher than that of the second reaction. Therefore, it is expected that the second Na site may generate more heat than the first Na site.

4. Conclusion

Si-modified $Na_{0.67}Mn_{0.5}Fe_{0.5}O_2$ samples were produced by quenching at high temperatures. The XRD patterns of the samples showed no impure peaks following an increase in Si content, but a broad halo around 10^o was observed, which may be due to the formation of an amorphous SiO_2 phase and the main phase was found to be $P_{63/mmc}$ symmetry. The surface photographs of the samples show that the amorphous SiO_2 coated on the $Na_{0.67}Mn_{0.5}Fe_{0.5}O_2$ grains after a certain amount of SiO_2 was added. The bonds with Si ions overlapped with the Fe–O, and Mn–O bonds in the FTIR spectra.It was found that Si modification in $Na_{0.67}Mn_{0.5}Fe_{0.5}O_2$ did not change the valence state of Fe and Mn ions. The structure of CV measurement did not change with Si modification and the best cycling performance was obtained for x=0.02. The XRD patterns of the Si-modified $Na_{0.67}Fe_{0.5}Mn_{0.5}O_2$ samples are almost the same properties and it was revealed by some part of Si

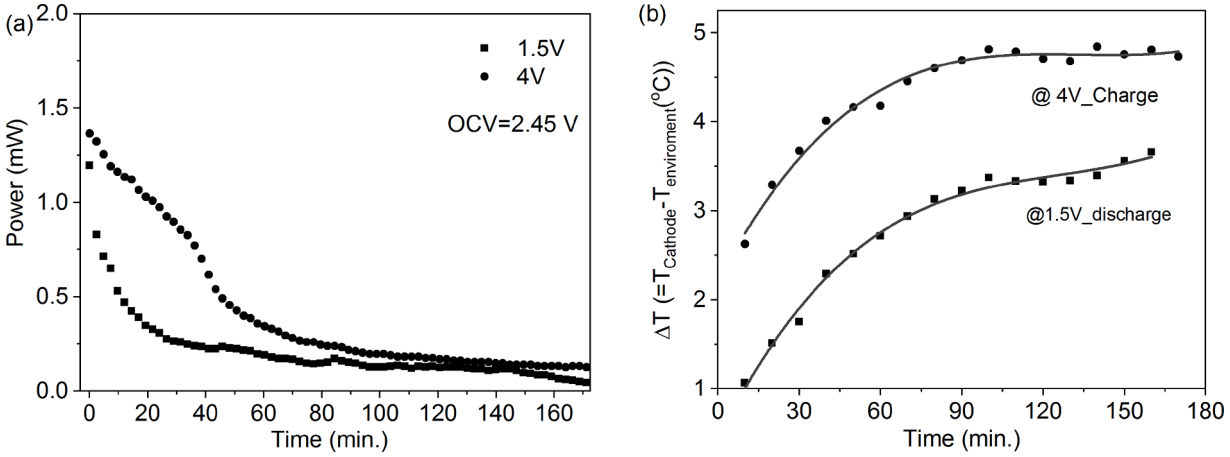
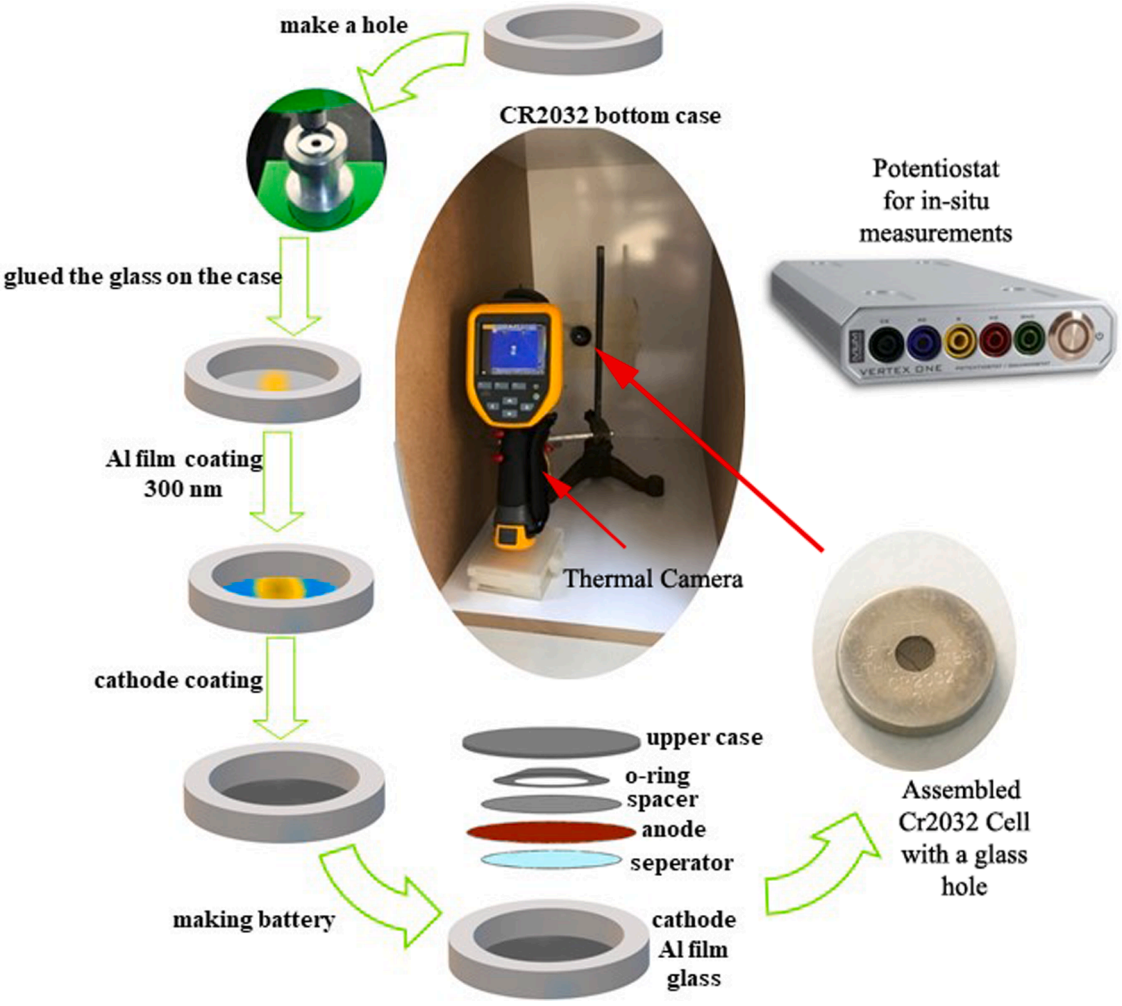


Fig. 10. Qohm-Time plot and ΔT-t measurements for charging and discharging of the cells.



Scheme 1. Cell design for IR-thermal imaging and experimental setup.

Table 3
The fitting parameters of the plots in Figure 10b.

Voltage	B_1	B_2	B_3	Adj.R-Square
1.5 V	0.061 ± 0.005	$-4.50 \times 10^{-4} \pm (0.60 \times 10^{-4})$	$1.189 \times 10^{-6} \pm (0.25 \times 10^{-6})$	0.99
4 V	0.058 ± 0.005	$-4.40 \times 10^{-4} \pm (0.66 \times 10^{-4})$	$1.097 \times 10^{-6} \pm (0.24 \times 10^{-6})$	0.98

dissolved in the lattice which caused the change of c/a ratio and the other parts may cause to cover of grains which increase the electrical conductivity of the grains. In this case, the electrochemical performance of the cells was affected for both situations.

In situ IR thermal imaging of the CR2032 coin cell was performed by a special design, as explained in Scheme 1 and it was found that the internal temperature was higher than the surface temperature of the cells. The heat exhibited a quadratic dependence which may give insights for thermal management studies of batteries. We predicted that the heat generation has multiple components which are effective for the value of the temperature gradient.

Declaration of Competing Interest

We declare that there is no conflict of interest in the study.

Acknowledgment

The authors would like to thank TUBITAK for financial support by contract number 119M169. Prof. S. Altin would like to thank SESAME for XAS experiments with project number 20185036. We also want to thank the EU CALIPSO program for traveling and accommodation support during to SESAME experiments. The study also supported by Inonu University Research Council by the project number of FYL-2020-2094.

Supplementary materials

Supplementary material associated with this article can be found, in the online version, at doi:10.1016/j.est.2021.102979.

References

[1] M. Woodya, M. Arbabzadeha, G.M. Lewisa, G.A. Keoleiana, A. Stefanopoulou, Strategies to limit degradation and maximize Li-ion battery service lifetime - Critical review and guidance for stakeholders, J. Energy Storage 28 (2020) 101–231, https://doi.org/10.1016/j.est.2020.101231.
[2] T.M. Clancy, J.F. Rohan, Simulations of 3D nanoscale architectures and electrolyte characteristics for Li-ion microbatteries, J. Energy Storage 23 (2019) 1–8, https://doi.org/10.1016/j.est.2019.02.002.
[3] L. Li, Y. Zheng, S. Zhang, J. Yang, Z. Shao, Z. Guo, Recent progress on sodium ion batteries: potential high-performance anodes, Energy Environ. Sci. 11 (2018) 2310–2340, https://doi.org/10.1039/C8EE01023D.
[4] T. Hou, Z. Jia, B. Wang, H. Li, X. Liu, L. Bi, G. Wu, MXene-based accordion 2D hybrid structure with Co9S8/C/Ti3C2Tx as efficient electromagnetic wave absorber, Chem. Eng. J. 414 (2021), 128875, https://doi.org/10.1016/j.cej.2021.128875.

[5] J. Cui, X. Chen, Z. Zhou, M. Zuo, Y. Xiao, N. Zhao, C. Shi, X. Guo, Effect of continuous pressures on electrochemical performance of Si anodes, Mater. Today Energy 20 (2021), 100632, https://doi.org/10.1016/j.mtener.2020.100632.

[6] C. Wang, B. Wang, X. Cao, J. Zhao, L. Chen, L. Shan, H. Wang, G. Wu, 3D flower-like Co-based oxide composites with excellent wideband electromagnetic microwave absorption, Composites Part B: Eng. 205 (2021), 108529, https://doi.org/10.1016/j.compositesb.2020.108529.

[7] Y. Zhang, Z. Wang, K. Hu, J. Ren, N. Yu, X. Liu, G. Wu, N. Liu, Anchoring silicon on the basal plane of graphite via a three-phase heterostructure for highly reversible lithium storage, Energy Storage Mater. 34 (2021) 311–319, https://doi.org/10.1016/j.ensm.2020.10.002.

[8] F. Zhang, Z. Jia, C. Wang, A. Feng, K. Wang, T. Hou, J. Liu, Y. Zhang, G. Wu, Sandwich-like silicon/Ti3C2Tx MXene composite by electrostatic self-assembly for high performance lithium ion battery, Energy 195 (2020), 117047, https://doi.org/10.1016/j.energy.2020.117047.

[9] J. Cui, Z. Zhou, M. Jia, X. Chen, C. Shi, N. Zhao, X. Guo, Solid polymer electrolytes with flexible framework of SiO2 nanofibers for highly safe solid lithium batteries, Polymers 12 (6) (2020) 1324, https://doi.org/10.3390/polym12061324.

[10] J.-ki Park, G.-gyung Park, H.H. Kwak, S.-T. Hong, J.-won Lee, Enhanced rate capability and cycle performance of titaniumsubstituted P2-type $Na_{0.67}Fe_{0.5}Mn_{0.5}O_2$ as a cathode for sodium-ion batteries, ACS Omega 3 (2018) 361–368, https://doi.org/10.1021/acsomega.7b01481.

[11] S. Chu, Y. Chen, J. Wang, J. Dai, K. Liao, W. Zhou, Z. Shao, A cobalt and nickel co-modified layered P2-$Na_{2/3}Mn_{1/2}Fe_{1/2}O_2$ with excellent cycle stability for high-energy density sodium-ion batteries, J. Alloys Compd. 775 (2019) 383–392, https://doi.org/10.1016/j.jallcom.2018.10.150.

[12] B.M. de Boisse, D. Carlier, M. Guignard, C. Delmas, Structural and electrochemical characterizations of P2 and new O3-$Na_xMn_{1-y}Fe_yO_2$ phases prepared by auto-combustion synthesis for Na-Ion batteries, J. Electrochem. Soc. 160 (2013) A569–A574, https://doi.org/10.1149/2.032304jes.

[13] H. Wang, Rui Gao, Z. Li, L. Sun, Z. Hu, X. Liu, Different effects of Al substitution for Mn or Fe on the structure and electrochemical properties of $Na_{0.67}Mn_{0.5}Fe_{0.5}O_2$ as a sodium ion battery cathode material, Inorg. Chem. 57 (2018) 5249–5257, https://doi.org/10.1021/acs.inorgchem.8b00284.

[14] J. Xu, S.-L. Chou, J.-L. Wang, H.-K. Liu, S.-X. Dou, Layered P2- $Na_{0.66}Fe_{0.5}Mn_{0.5}O_2$ cathode material for rechargeable sodium-ion batteries, ChemElectroChem. 1 (2) (2013) 371–374, https://doi.org/10.1002/celc.201300026.

[15] E. Altin, S. Altundag, S. Altin, A. Bayri, Fabrication of Cr doped $Na_{0.67}Fe_{0.5}Mn_{0.5}O_2$ compounds and investigation of their structural, electrical, magnetic and electrochemical properties, J. Mater. Sci. Mater. Electron. (2019), https://doi.org/10.1007/s10854-019-02136-9.

[16] N. Yabuuchi, M. Kajiyama, J. Iwatate, H. Nishikawa, S. Hitomi, R. Okuyama, R. Usui, Y. Yamada, S. Komaba, P2-type $Na_x[Fe_{1/2}Mn_{1/2}]O_2$ made from earth-abundant elements for rechargeable Na batteries, Nat. Mater. 11 (2012) 512–517, https://doi.org/10.1038/nmat3309.

[17] Y. Bai, L. Zhao, C. Wu, H. Li, Y. Li, F. Wu, Enhanced sodium ion storage behavior of P2-Type $Na_{2/3}Fe_{1/2}Mn_{1/2}O_2$ synthesized via a chelating agent assisted route, ACS Appl. Mater. Interfaces 8 (2016) 2857–2865, https://doi.org/10.1021/acsami.5b11848.

[18] E. Talaie, V. Duffort, H.L. Smith, B. Fultz, L.F. Nazar, Structure of the high voltage phase of layered P2-$Na_{2/3-z}[Mn_{1/2}Fe_{1/2}]O_2$ and the positive effect of Ni substitution on its stability, Energy Environ. Sci. 8 (2015) 2512–2523, https://doi.org/10.1039/c5ee01365h.

[19] R. Zhang, Y. Cui, W. Fan, G. He, X. Liu, Ambient stable $Na_{0.76}Mn_{0.48}Ti_{0.44}O_2$ as anode for Na-ion battery, Electrochim. Acta 295 (2018) 181–186, https://doi.org/10.1016/j.electacta.2018.10.126.

[20] G. Singh, J.M. López del Amo, M. Galceran, S. Pérez-Villar, T. Rojoa, Structural evolution during sodium deintercalation/intercalation in $Na_{2/3}[Fe_{1/2}Mn_{1/2}]O_2$, J. Mater. Chem. 3 (2015) 6954–6961, https://doi.org/10.1039/c4ta06360k.

[21] M.H. Han, B. Acebedo, E. Gonzalo, P.S. Fontecoba, S. Clarke, D. Saurel, T. Rojoa, Synthesis and electrochemistry study of P2- and O3-phase $Na_{2/3}Fe_{1/2}Mn_{1/2}O_2$, Electrochim. Acta 118 (2015) 1029–1036, https://doi.org/10.1016/j.electacta.2015.10.003.

[22] R. Viswanatha, B. Kishore, U. Bharath, N. Munichandraiah, Communication—electrochemical investigation of plate-Like $Na_{2/3}Fe_{1/2}Mn_{1/2}O_2$ for sodium ion cathode, J. Electrochem. Soc. 165 (2018) A263–A265, https://doi.org/10.1149/2.0911802jes.

[23] D. Darbar, N. Muralidharan, R.P. Hermann, J. Nanda, I. Bhattacharya, Evaluation of electrochemical performance and redox activity of Fe in Ti doped layered P2-Na0.67Mn0.5Fe0.5O2 cathode for sodium ion batteries, Electrochim. Acta 380 (2021), 138156, https://doi.org/10.1016/j.electacta.2021.138156.

[24] Y. Sui, Y. Hao, X. Zhang, J. Li, G. Wen, S. Zhong, Z. Zhang, L. Wu, Improved electrochemical properties of vanadium substituted Na0•67Fe0•5Mn0•5O2 cathode material for sodium-ion batteries, Ceram. Int. 47 (2021) 5227–5234, https://doi.org/10.1016/j.ceramint.2020.10.102.

[25] V.K. Kumar, S. Ghosh, S. Biswas, S.K. Martha, P2-type Na0.67Mn0.5Fe0.5O2 synthesized by solution combustion method as an efficient cathode material for sodium-ion batteries, J. Electrochem. Soc. 168 (2021), 030512, https://doi.org/10.1149/1945-7111/abe985.

[26] S. Altin, A. Bayri, E. Altin, S.Yasar E.Oz, S. Altundag, M. Harfouche, S. Avci, Magnetic properties and environmental temperature effects on battery performance of Na0.67Mn0.5Fe0.5O2, Energy Technol (2021), 2001130, https://doi.org/10.1002/ente.202001130.

[27] M. Li, D.L. Wood, Y. Bai, R. Essehli, M.R. Amin, C. Jafta, N. Muralidharan, J. Li, I Belharouak, Eutectic synthesis of the P2-Type NaxFe1/2Mn1/2O2 cathode with improved cell design for sodium-ion batteries, ACS Appl. Mater. Interfaces 12 (2020) 23951–23958, https://doi.org/10.1021/acsami.0c04513.

[28] T. Adhikari, A. Hebert, M. Adamic, J. Yao, K. Potts, E. McCalla, Development of high-throughput methods for sodium-ion battery cathodes, ACS Comb. Sci. 22 (2020) 311–318, https://doi.org/10.1021/acscombsci.9b00181.

[29] W. Kong, W. Yang, D. Ning, Q. Li, L. Zheng, J. Yang, K. Sun, D. Chen, X. Liu, Tuning anionic/cationic redox chemistry in a P2-type Na0.67Mn0.5Fe0.5O2 cathode material via a synergic strategy, Sci. China Mater. 63 (2020) 1703–1718, https://doi.org/10.1007/s40843-020-1318-4.

[30] B.H. Toby, EXPGUI, a graphical user interface for GSAS, J. Appl. Cryst. 34 (2001) 210–213, https://doi.org/10.1107/S0021889801002242.

[31] B.H. Toby, R.B. Von Dreele, GSAS-II: the genesis of a modern open-source all purpose crystallography software package, J. Appl. Cryst. 46 (2013) 544–549, https://doi.org/10.1107/S0021889813003531.

[32] A.V. Llewellyn, A. Matruglio, D.J.L. Brett, R. Jervis, P.R. Shearing, Using In-Situ laboratory and synchrotron-based X-ray diffraction for lithium-ion batteries characterization: a review on recent developments, Condens. Matter 5 (2020) 75, https://doi.org/10.3390/condmat5040075.

[33] M. Sommerfeld, S. Schmalfu, Analysis and optimisation of particle mixing performance in fluid phaseresonance mixers based on Euler/Lagrange calculations, Adv. Powder Technol. 31 (2020) 139–157, https://doi.org/10.1016/j.apt.2019.10.006.

[34] S. Pani, S.K. Singh, B.K. Mohapatra, Vibrational spectroscopic study for qualitative assessment of Mn-oxide Ore, Resour. Geol. 66 (2016) 12–23, https://doi.org/10.1111/rge.12083.

[35] A.P. dos Santos Pereira, M.H.P. da Silva, É.P.L. Júnior, A. dos Santos Paula, F. J. Tommasini, Processing and characterization of PET composites reinforced with geopolymer concrete waste, Mater. Res. 20 (2017) 411–420, https://doi.org/10.1590/1980-5373-MR-2017-0734.

[36] M. Dimitrakopoulou, X. Huang, J. Krohnert, D. Teschner, S. Praetz, C. Schlesiger, W. Malzer, C. Janke, E. Schwab, F. Rosowski, H. Kaiser, S. Schunk, R. Schlogl, A. Trunschke, Insights into structure and dynamics of $(Mn,Fe)O_x$-promoted Rh nanoparticles, Faraday Discuss 208 (2018) 207–225, https://doi.org/10.1039/c7fd00215g.

[37] NIST Standard Reference Database Number 69, https://doi.org/10.18434/T4D303.

[38] E. Herth, R. Zeggari, J.-Y. Rauch, F. Remy-Martin, W. Boireau, Investigation of amorphous SiOx layer on gold surface for Surface Plasmon Resonance measurements, Microelectron. Eng. 163 (2016) 43–48, https://doi.org/10.1016/j.mee.2016.04.014.

[39] S. Altin, S. Altundağ, E. Altin, M. Harfouche, A. Bayri, An investigation of the improvement in energy storage performance of $Na_{2/3}Mn_{1/2}Fe_{1/2}O_2$ by systematic Al-substitution, J. Mater. Sci. Mater. Electron. 31 (2020) 14784–14794, https://doi.org/10.1007/s10854-020-04042-x.

[40] S. Altin, S. Altundag, E. Altin, E. Oz, M. Harfouche, A. Bayri, Investigation of Ti-substitution effects on structural and electrochemical properties of $Na_{0.67}Mn_{0.5}Fe_{0.5}O_2$ battery cells, Int. J. Energy Res (2020) 1–13, https://doi.org/10.1002/er.5820.

[41] M. Guan, J. Chen, X. Zhang, L. Yang, B. Wang, S. Zhong, Yarn-ball-shaped P2-$Na_{2/3}Fe_{1/2}Mn_{1/2}O_2$ nanofibers prepared by magnetic-assisted electrospinning method as high-performance cathode material for Na-ion batteries, Mater. Lett. 254 (2019) 24–27, https://doi.org/10.1016/j.matlet.2019.07.001.

[42] J. Chen, S. Zhong, X. Zhang, J. Liu, S. Shi, Y. Hu, L. Wu, High performance of hexagonal plates P2-$Na_{2/3}Fe_{1/2}Mn_{1/2}O_2$ cathode material synthesized by an improved solid-state method, Mater. Lett. 202 (2017) 21–24, https://doi.org/10.1016/j.matlet.2017.05.084.

[43] A.J. Naylor, E. Makkos, J. Maibach, N. Guerrini, A. Sobkowiak, E. Björklund, J. G. Lozano, A.S. Menon, R. Younesi, M.R. Roberts, K. Edström, M.S. Islam, P. G. Bruce, Depth-dependent oxygen redox activity in lithium rich layered oxide cathodes, J. Mater. Chem. A 7 (2019) 25355, https://doi.org/10.1039/c9ta09019c.

[44] T. Famprikis, P. Canepa, J.A. Dawson, M.S. Islam, C. Masquelier, Fundamentals of inorganic solid-state electrolytes for batteries, Nat. Mater. 18 (2019) 1278–1291, https://doi.org/10.1038/s41563-019-0431-3.

[45] R. Sharpe, R.A. House, M.J. Clarke, D. Förstermann, J-J. Marie, G. Cibin, K-J. Zhou, H.Y. Playford, P.G. Bruce, M.S. Islam, Redox chemistry and the role of trapped molecular O2 in Li-Rich disordered rocksalt oxyfluoride cathodes, J. Am. Chem. Soc. 142 (2020) 21799–21809, https://doi.org/10.1021/jacs.0c10270.

[46] N. Tapia-Ruiz, W.M. Dose, N. Sharma, H. Chen, J. Heath, J.W. Somerville, U. Maitra, M.S. Islam, P.G. Bruce, High voltage structural evolution and enhanced Na-ion diffusion in P2-Na2/3Ni1/3xMgxMn2/3O2 (0 r x r 0.2) cathodes from diffraction, electrochemical and ab initio studies, Energy Environ. Sci. 11 (2018) 1470, https://doi.org/10.1039/c7ee02995k.

[47] Y. Yang, Z. Wang, J. Jiang, H. Bian, N. Mao, L. Guo, Effects of different charging and discharging modes on thermal behavior of lithium ion batteries, Fire Mater. (2019) 1–10, https://doi.org/10.1002/fam.2778.

[48] N. Sato, Thermal behavior analysis of lithium-ion batteries for electric and hybrid vehicles, J. Power Sources 99 (2001) 70–77, https://doi.org/10.1016/S0378-7753(01)00478-5.

[49] R. Christen, G. Rizzo, A. Gadola, M. Stöck, Test Method for thermal characterization of li-ion cells and verification of cooling concepts, Batteries 3 (2017), https://doi.org/10.3390/batteries3010003, 3.

[50] Y. Abdul-Quadir, T. Laurila, J. Karppinen, K. Jalkanen, K. Vuorilehto, L. Skogström, M. Paulasto-Kröckel, Heat generation in high pow er prismatic Li-ion batterycell with $LiMnNiCoO_2$ cathode material, Int. J. Energy Res. 38 (2014) 1424–1437, https://doi.org/10.1002/er.3156.

[51] G. Liu, M. Ouyang, L. Lu, J. Li, X. Han, Analysis of the heat generation of lithium-ion battery during charging and discharging considering different influencing factors, J. Therm. Anal. Calorim 116 (2014) 1001–1010, https://doi.org/10.1007/s10973-013-3599-9.

[52] F. He, X. Li, L. Ma, Combined experimental and numerical study of thermal management of battery module consisting of multiple Li-ion cells, Int. J. Heat Mass Transfer 72 (2014) 622–629, https://doi.org/10.1016/j.ijheatmasstransfer.2014.01.038.

[53] V. Duffort, E. Talaie, R. Black, L.F. Nazar, Uptake of CO_2 in Layered P2-$Na_{0.67}Mn_{0.5}Fe_{0.5}O_2$: insertion of carbonate anions, Chem. Mater. 27 (2015) 2515–2524, https://doi.org/10.1021/acs.chemmater.5b00097.

[54] C. Ding, T. Nohira, R. Hagiwara, Charge-discharge performance of $Na_{2/3}Fe_{1/3}Mn_{2/3}O_2$ positive electrode in an ionic liquid electrolyte at 90 °C for sodium secondary batteries, Electrochim. Acta 231 (2017) 412–416, https://doi.org/10.1016/j.electacta.2017.02.069.

[55] E. Marelli, C. Villevieille, S. Park, N. Hérault, C. Marino, Co-Free P2-$Na_{0.67}Mn_{0.6}Fe_{0.25}Al_{0.15}O_2$ as promising cathode material for sodium ion batteries, ACS Appl. Energy Mater. 1 (2018) 5960–5967, https://doi.org/10.1021/acsaem.8b01015.